Journal Name

Nanoscale Mechanics of Microgel Particles[†]

Anders Aufderhorst-Roberts,[ab] Daniel Baker,[b] Richard J Foster,[b] Olivier Cayre,[c] Johan Mattsson[b] and Simon D Connell[b*]

Microgel particles are highly tuneable materials that are useful for a wide range of industrial applications, such as drug delivery, sensing, nanoactuation, emulsion stabilisation and use as cell substrates. Microgels have also been used as model systems investigating physical phenomena such as crystallization, glass-formation, jamming, ageing and complex flow behaviour. The responsiveness of microgel systems such as poly(N-isopropylacrylamide) (PNIPAm) to external stimuli has been established in fundamental investigations and in applications and recent work has begun to quantify the mechanics of individual particles. However little focus has been placed on determining their internal mechanical properties, which is likely to relate to their nonuniform internal structure. In this work we combine atomic force microscopy, force spectroscopy and dynamic light scattering to mechanically profile the internal structure of microgel particles in the size range of ∼ 100nm, which is commonly used both in practical applications and in fundamental studies. Nanoindentation using thermally stable cantilevers allows us to determine the particle moduli and the deformation profiles during particle compression with increasing force, while peak force nanomechanical mapping (PF-QNM) AFM is used to capture high resolution images of the particles' mechanical response. Combining these approaches with dynamic light scattering allows a quantitative profile of the particles' internal elastic response to be determined. Our results provide clear evidence for a radial distribution in particle mechanical response with a softer outer "corona" and a stiffer particle core. We determine the particle moduli in the core and corona, using different force microscopy approaches, and find them to vary systematically both in the core (∼17-50kPa) and at the outer periphery of the particles (∼3-40kPa). Importantly, we find that highly crosslinked particles have equivalent moduli across their radial profile, reflecting their significantly lower radial heterogeneity. This ability to accurately and precisely probe microgel radial profiles has clear implications both for fundamental science and for industrial applications.

1 Introduction

Microgels are swollen polymer spheres that can be assembled from simple chemical components but nevertheless possess sur-

[a] AMOLF, 1098 XG Amsterdam, The Netherlands

[b] School of Physics and Astronomy, University of Leeds, Leeds LS2 9JT, United Kingdom; E-mail: S.D.A.Connell@leeds.ac.uk>

[c] School of Chemical and Process Engineering, University of Leeds, Leeds LS2 9JT, United Kingdom

† Electronic Supplementary Information (ESI) available: intensity autocorrelation, g_2, as a function of measured lag time, τ for all CMRs (Fig. S1), mean hydrodynamic radius R_h with respect to CMR (Table S1), low force contact mode images and averaged cross sections of particles (Fig. S2), example force vs. indentation curve (1× CMR), showing the approach used to determine the contact point (Fig. S3), force vs. indentation curves overlaid with corresponding Hertz model fits (Fig. S4), particle heights at particle centre at variable force (S5) and extrapolated particle profile taken from peak force QNM AFM (Fig. S6). Original data available at DOI: 10.5518/394

prisingly complex structural and mechanical properties.[1] Their structures are highly sensitive to stimuli such as temperature and ionic strength and this sensitivity can be precisely tuned using different polymerisation methodologies to control crosslink density, polydispersity or the incorporation of co-monomers.[2] This combination of *sensitivity* and *versatility* makes them ideal for a range of proposed applications, which include drug delivery,[3] sensing,[4] nanoactuation,[5] emulsion stabilisation,[6] lubrication,[7] cell encapsulation[8] and their use as cell substrates.[9] They are also of interest from a fundamental perspective as model systems for the study of phenomena such as structural relaxation, glass formation,[10,11,12] crystallisation[13,11,14], jamming[15], dynamic heterogeneity[16] and complex flow behaviours.[17,18,11]

A topic of central interest in the application of microgels relates to the relationship between the properties of microgel dispersions and the characteristics of the constituent individual microgel par-

ticles.[18] However, quantitatively determining the mechanics of individual microgel particles is challenging as their inherently soft response requires experimental techniques that are able to measure forces on the order of pN.[19] One approach that has been identified as successful is to extract the compressive elastic modulus from the volume changes induced by a set range of osmotic pressures.[20] A more recent method is to determine the deformations induced in a microgel particle that is pushed into a tapered micro-capilary by a controlled external pressure.[21] This method can determine both compressive and shear moduli from optically determining the resulting particle deformations. However it approximates the particles as elastically isotropic and is limited to larger particles that can be imaged using an optical microscope. Atomic force microscopy (AFM) is also able to extract the particles' Young's modulus using nano-indentation. AFM imaging and nanoindentation have so far been mostly limited to large[22] and stiff ($\sim$100kPa[23]-1MPa[22]) particles, which are generally homogeneous. For softer particles imaging with sharp AFM probes can be challenging, with adverse effects from tip-sample adhesion and results that are sensitive to small changes in imaging parameters.[24]

A common solution to studying very soft samples, such as the surface of cells, is to modify the AFM tip by attaching a micron-sized colloidal particle,[25, 26] sacrificing lateral resolution in favour of force sensitivity. This broad probe contact area results in a lack of sensitivity to internal heterogeneities that are smaller than the probe. Thus there are, to the best of our knowledge, no reports of high resolution profiling of the *internal* elastic properties of soft microgel particles. Small angle neutron scattering[27, 28, 29, 30, 31] experiments have established that there exists a radial gradient in polymer density within poly (N-isopropylacrylamide) (PNIPAm)-based microgel particles synthesized using emulsion polymerization, as expected from the difference in the monomer and crosslinker reaction rates.[31] More recently, super-resolution microscopy has been used to directly visualise this morphology in PNIPAm microgels with the measured internal structure being in close agreement with values measured in scattering experiments.[32].

Here, we report on a new approach to determining the radially dependent structure and elasticity of sub-micron sized microgel particles. Chemically crosslinked pNIPAM microgel particles are widely studied as model systems and for practical applications. The fact that pNIPAM microgels undergo a thermally induced reversible volume transition at temperatures of $\sim$32° makes it useful in many applications and as a versatile model system. We here probe the mechanics of a series of chemically crosslinked pNIPAM microgel particles with systematically varied crosslink-monomer-ratio (CMR). We probe the microgel particle mechanics using AFM with "DC MLCT-BIO" cantilevers, chosen for their low spring constant (0.01-0.6N/m) and special back coating which results in high thermal stability (for example in relation to heating from the back-reflected laser). This combination of low spring constant and high stability means that the applied force can be precisely controlled which minimises damage to the sample and eliminates the need for colloidal probes. We use standard nano-indentation techniques (so-called force-volume mode AFM), to determine the applied force as a function of resulting cantilever displacement, which enables us to probe the elasticity in a spatially resolved manner. We also use the more recent innovation of peak force quantitative nanomechanical mapping (PF-QNM), which captures force-distance curves at significantly faster acquisition speeds, analysing them in real time rather than capturing raw data, to extract a microgel particle's local modulus, adhesion, and deformation. The validity of PF-QNM has previously been confirmed on a range of soft and biological materials including amyloid fibrils[33], lipid bilayers,[34, 35] and algae[36] but has yet to be used to characterise microgel particles.

We combine force-volume and PF-QNM mode AFM to profile the internal structure and elasticity of PNIPAMm microgel particles with radii on the 100nm scale, significantly smaller than those studied in the literature to date. From the former mode, we ultilise the ability to capture entire force curves to measure the modulus at the particle periphery and compile an averaged radial profile illustrating how the microgel particles compress in response to an applied force. From the latter mode we utilize its high throughput advantage to capture high resolution images of the lateral structure at different applied force and extract the particle moduli, adhesion and deformations at higher applied force. Combining these techniques with information about the hydrodynamic radii, determined using dynamic light scattering, allows us to determine the radially varying elastic particle properties for microgels of varying CMRs.

2 Materials and Methods

2.1 PNIPAm microgel Synthesis

Colloidal suspensions of PNIPAm, chemically crosslinked with N,N'methylenbisacrylamide (BIS), were prepared using standard emulsion polymerization protocols.[37] Specifically, NIPAm monomer (2.361g), SDS stabiliser (0.045g) and varying amounts of BIS crosslinker (0.045g-0.27g) were dissolved in 135ml of MilliQ water. The solutions were transferred into 3-necked flasks containing stirrer bars and gas inlets and connected to a reflux condenser before being bubbled with nitrogen for 30 minutes. The mixtures were then heated to 70°C under stirring at 350rpm. Solutions of KPS initiator (0.09g) in 15ml of MilliQ water were added drop-wise to the other reactants. The polymerization process took place over a course of 24 hours, after which the suspensions were cooled to room temperature and subsequently filtered using glass wool. Further purification of the suspensions was achieved through dialysis of each suspension against milli-Q water, using dialysis membrane tubing with a 12-14kDa molecular weight cutoff. The dialysis was conducted for 2 weeks, with an exchange of water every 24 hours.

Microgels were prepared using four different synthesis protocols, which varied according to the amount of added crosslinker. For 2.361g of PNIPAm monomer (M$_w$=113.16) and 0.045g of BIS crosslinker (M$_w$=154.17), the resulting monomer-to-crosslink molar ratio (CMR) was therefore 71.5. For convenience, in the following, the microgels prepared using this protocol are termed '1$\times$'. Correspondingly, the microgels prepared using twice as much crosslinker are termed '2$\times$', those with with four times

as much crosslinker are termed '4×' and those with six times as much cross-linker as '6×'.

2.2 Dynamic Light Scattering

Dynamic light scattering (DLS) measurements were performed using a photocorrelation spectrometer from LS Instruments with a HeNe laser excitation wavelength of 632.8nm. Dilute microgel suspensions ($\sim 10^{-4}$-10^{-5} wt%) were placed into 10mm inner diameter glass tubes. For the sizing measurements, the scattered light was detected at a scattering angle of $\theta = 90°$. The intensity correlation function g_2 was determined from the time-dependent scattered intensities. The g_2 data were fitted using a cumulant expression (expanded to the second cumulant) of the form:[38]

$$g_2 = 1 + \Omega e^{(-2\bar{\Gamma}\tau)} \left(1 + \frac{\mu_2}{2!}\tau^2\right)^2. \quad (1)$$

Here, Ω is a set-up dependent coherence factor: for our spectrometer $\Omega \approx 0.95$ and μ_2 is the second moment about the mean of the relaxation rate. The relaxation rate Γ is directly related to the particle self diffusion coefficient D, as $\Gamma = DQ^2$, where $Q = 4\pi n/\lambda \sin(\theta/2)$, where λ is the wavelength, and θ is the scattering angle. After determining D through fits of the g_2 data, the Stokes-Einstein equation was used in order to calculate the hydrodynamic radius, R_h:

$$D = \frac{k_B T}{6\pi\eta R_h}, \quad (2)$$

where k_B is the Boltzmann constant, T is the temperature and η is the viscosity.

2.3 Atomic Force Microscopy

Microgel suspensions were diluted by a factor of 100 using MilliQ water and 100μl aliquots were pipetted on to a silicon wafer substrate. In order to ensure a strong adsorption of the microgel particles onto the substrate, contaminants were first removed from the surface through washing multiple times with jets of Milli-Q water and methanol. The clean surface was immediately dried using an air gun and no further surface treatment was necessary. The samples were incubated in a hydrated state for 10 minutes at room temperature and rinsed 5 times with 100μl of MilliQ water using a micropipette to remove non-adsorbed particles from the suspension that could otherwise adhere to the AFM cantilever tip. Samples were then transferred to AFM for imaging and kept in a hydrated state at all times.

Atomic force microscopy was carried out using a Bruker Multimode 8 AFM with a Nanoscope V controller using Bruker mlc probes, specifically the C and D probes (nominal spring constants of 0.01 and 0.03 N/m, respectively). Low spring constant cantilevers are normally very susceptible to thermal drift hence precise force control is difficult. This cantilever design utilizes a reflective coating only on the cantilever apex, with the uncoated legs no longer susceptible to the usual bimetallic strip effect, resulting in a thermally stable probe.

Cantilever spring constants were determined through the thermal noise method.[39] The cantilever tips have a radius of $\approx$ 30nm, measured directly for each experiment using a polycrystalline ti-
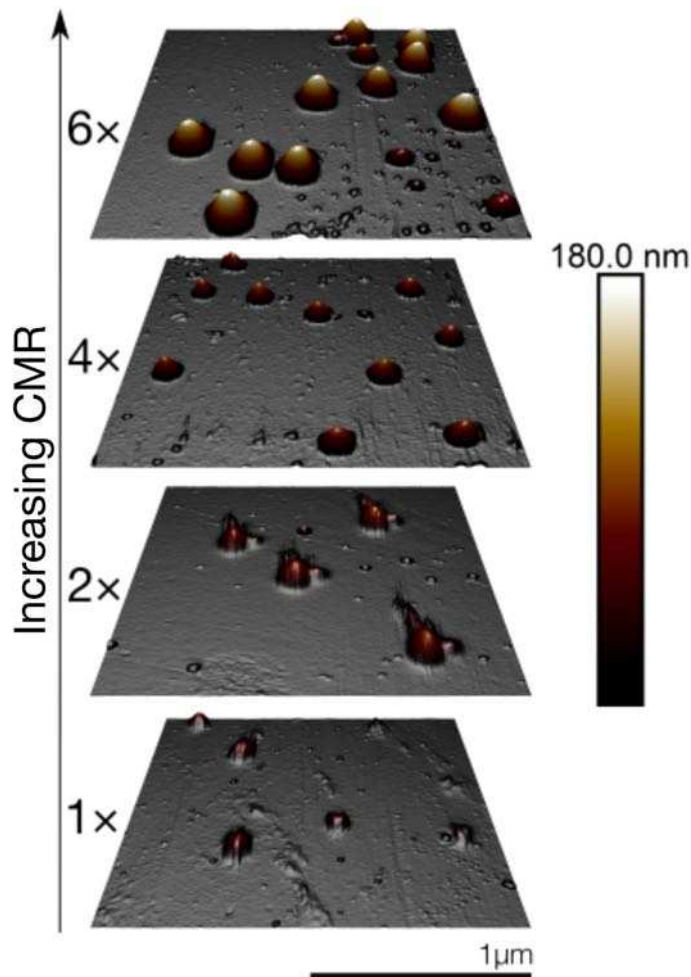

Fig. 1 PNIPAm particles imaged using contact mode AFM. The low contact force and soft, stable cantilevers allow the particles to be spatially profiled at high resolution. However the apparent decrease in particle size with decreasing CMR (opposite to the trend shown in figure S1) suggests that, even at low forces, lower CMR particles are disproportionately compressed by the AFM tip. Images are rendered in 3D with a 0.15 aspect ratio in the z-direction for clarity.

tanium characteriser sample and the "Tip Qualification" function in Nanoscope Analysis 1.8. Cantilevers were cleaned thoroughly with water, detergent and methanol at 2 hour intervals of imaging to prevent build up of debris on the tip surface. Before imaging, the sample was kept within the AFM chamber for 10 minutes to allow the temperature to equilibrate. The temperature within the chamber was measured as 28°C.

When operating in force volume mode, the C probe of the MLCT-BIO-DC was used and force curves were captured at a rate of 4.3Hz, with a ramp size of 600nm. When operating in peak force QNM mode the D probe of the MLCT-BIO-DC was used and the cantilever was oscillated at 250Hz, lower than the standard frequency of 2kHz, at an amplitude of 300nm. We found that this combination of high force ramp amplitudes, stable cantilevers and low oscillation frequency resulted in the highly stable and reproducible force curves necessary for this approach.

3 Results

3.1 Hydrodynamic Radii

The intensity autocorrelation data, $g_2 - 1$ as a function of measured lag time, τ for the different microgel suspensions are shown in Figure S1. These data have been renormalised by the coherence factor, Ω, and were taken at a temperature of $28°C$, the same as the measured temperature within the AFM chamber. The lines are the results of fits to each data set using a cumulant expression. The characteristic timescales at which the autocorrelation functions decay are indicative of the sizes of the particles within the suspensions: particles with larger hydrodynamic radii (e.g. the $1 \times$ suspension) will have a lower diffusion coefficient and thus have a longer characteristic timescale. The inset of figure S1 shows the hydrodynamic radii as calculated from equation 2 together with the standard deviations $= \sqrt{(\mu_2/\overline{\Gamma}^2)}$.[40] The resulting R_h values are listed in table S1.

3.2 Soft Contact Mode Imaging

Microgel particles were imaged using contact mode AFM with a low cantilever deflection setpoint. This so-called "soft contact" imaging was found to yield higher quality images than tapping mode AFM. We believe this is due to a coupling between the cantilever's acoustic drive frequency and the surface of the soft elastic particles, driving resonances which cause instabilities in the feedback mechanism. Figure 1 shows a three dimensional rendering of atomic force micrographs of each of the four particle suspensions.

For each of the suspensions the particle profile is observed to be smooth and parabolic in shape. The substrate surface shows evidence of some debris, possibly remaining SDS stabiliser in the bulk.[41] The sharp, well resolved profile of the debris on the surface is strong evidence that the contrasting smooth shape of the microgel particles is not an artifact caused by tip deconvolution but a true representation of the highly smooth particle profile.

The measured particle height in each of the images appears to decrease with decreasing crosslink concentration, precisely the opposite trend as that observed in the hydrodynamic radii, as determined using DLS in figure S1. We interpret this as being a consequence of the microgel particles being compressed by the forces applied by the cantilever tip. Particles with lower CMR can be expected to be softer and more deformable as a consequence, causing them to appear smaller. Although contact mode can allow fine control of force if there is no tip-sample adhesion and low thermal drift of the cantilever (as with MLCT-BIO-DC probes), the slow response time of these long cantilevers at low forces («100pN) result in a slow response of the feedback loop. This slow response adversely affects image resolution, necessitating low scan speeds and resultant high levels of image lateral drift. Nonetheless, lowering this force further to around 50pN causes the particles to appear taller, but at the expense of image resolution and imaging stability. For the least deformable particles ($6\times$), at this low force, the measured height and the radius, defined as the half width at half maximum, were observed to be approximately equal, as shown in Fig. S2 of the supplementary information. Although tip deconvolution at this low force makes these measurements imprecise, the fact that the height and radius are approximately equivalent suggests that the particles adopt a hemispherical morphology when adsorbed to the surface. This observation contrasts to previous reports of stiffer ($\sim$1MPa) PNIPAm particles where a flat pancake-like morphology was observed, albeit with stiffer cantilevers than those used in this study.[22] For softer particles (lower CMR), the particles no longer appear hemispherical even at reduced force, an indication that it is not possible to accurately profile these softer particles using standard contact mode imaging.

3.3 Force-Volume AFM

The varying deformability between particles with different CMRs clearly indicates a variability in mechanical properties. To quantify this we used nano-indentation on individual particles by performing a simple loading test with the AFM tip, so-called "force-volume" mode AFM (Figure 2A). This provides multiple force measurements on individually identifiable microgels, as well as the surrounding clean silicon surface for reference. Between 3 and 7 microgel particles were analysed for each CMR, with 16 force curves from the central region of each microgel particle extracted by drawing a 4x4 pixel sample box in Nanoscope Analysis v1.9. Each particle was approximately 12 pixels in diameter so the 4 pixel-width reliably corresponded to the particle centre, thereby avoiding edge effects. The z-piezo vs. tip deflection curves were converted to tip sample separation by subtracting the linear response against a hard surface. Whilst this was pre-calibrated on sapphire, the long acquisition times of the force maps led to a small drift in deflection sensitivity, so this was recalibrated in each individual map from the response of the cantilever on the background silicon substrate close to the particle being measured. This could lead to a correction of several nm/V with a typical sensitivity of 65 nm/V. The ability to internally calibrate largely negates the problems caused by errors in deflection sensitivity which has recently been shown to introduce the largest relative error in force spectroscopy.[42] Deflection was converted to force by multiplying with the thermally calibrated spring constant of each cantilever (typically around 0.011 N/m).

Prior to contact with the surface the force is negligible with a flat baseline, demonstrating the thermal stability of the soft cantilever (the DC offset from the constant hydrodynamic drag force has already been subtracted by a linear fit in a region of approximately 20%-60% of the ramp size). The thermal noise baseline in the force is approximately 30pN peak-to-peak, as expected. Thermal noise is also observed during sample indentation, implying that the microgel is itself fluctuating. For indentation the contact point must be determined, but in soft contact this is very difficult to determine and a persisting issue that is still the subject of research.[43,44] In brief, our approach recognises that most contact models reduce to a power law, hence a log-log plot will result in a straight line. As the zero-force baseline has already been corrected, half of the zero force data will lie at negative force and not be plotted. To find the contact point we extrapolate the linearised indentation curve to a force level of 1pN as shown in figure S3 of
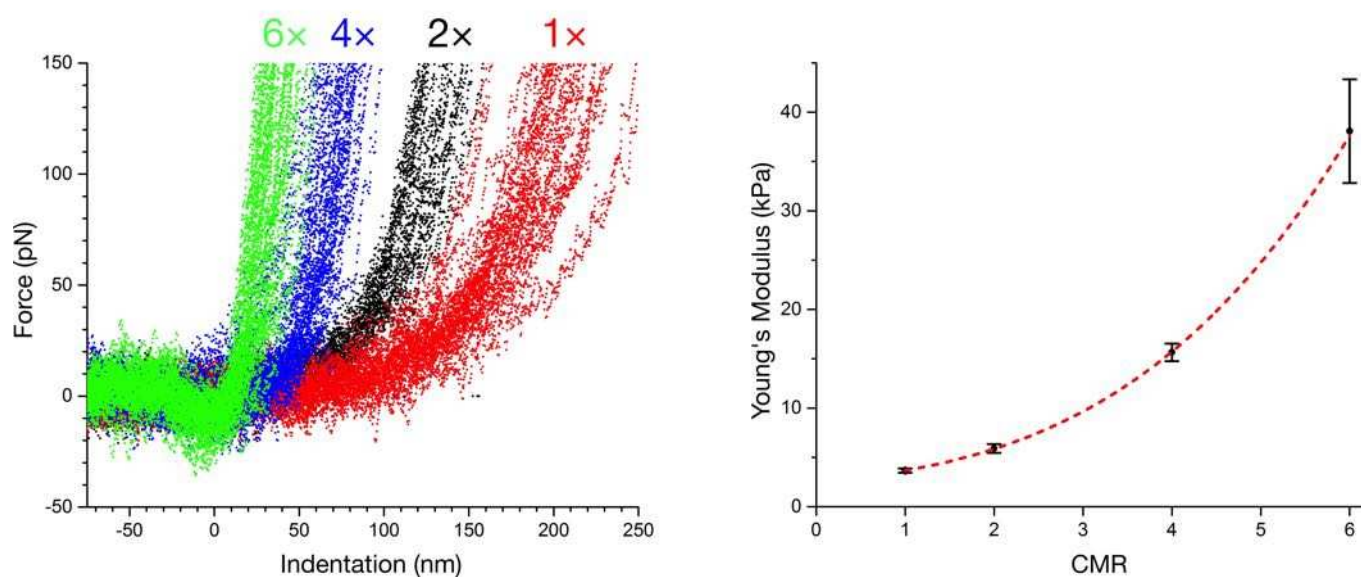
Fig. 2 Plots of force vs. indentation at the centres of individual PNIPAm microgel particles .(A) Force curves are fitted using the Hertz model (red) at low force ($< 50pN$) to give moduli (B) within the $\approx$3-40 kPa range for all CMRs, with higher CMRs resulting in higher moduli. Moduli increase with power law of exponent 3 (dashed line).

the supplementary information. This method avoids arguments over which contact model is most suitable. Once the zero contact point is fixed we fit the indentation curve to the Hertz model, having a power law exponent of 3/2, with the only free parameter being the modulus.

The Hertz model is the simplest contact mechanics model, describing a spherical cap indenting a flat plane. However, it must be acknowledged that the applicability of the Hertz model to microgels is a matter of debate, and other models could be applied. The most important parameter is whether the gel conforms locally to the probe. Where the Hertz model assumes a relatively stiff surface being deformed a small distance by the spherical end of the probe, the Sneddon model assumes the material is soft and conforms to the geometry of the deeply penetrating probe, molding around it completely, leading to a power law exponent of 2. Alternatively it could be modelled as a neo-Hookean response at high strains, with the microgel deforming across its entire volume as an elastic sphere between two hard planes. In this work, we found that application of the Sneddon model, despite its very different parameters, only results in a slight increase in modulus across all samples. A further point of contention is whether the probe is not indenting and deforming the microgel particle, but is rather penetrating through the porous crosslinked polymer. Unfortunately this would produce a similar power-law force response due to the interaction volume increasing according to the geometry of the indenting probe. Evidence against this possibility comes in two forms. Firstly, the retract force curves exactly follow the indentation curve: there is no hysteresis, indicating no plastic deformation and a purely elastic response. If bonds were being broken this would not be the case. Secondly, our probes have tip radii of the order 30nm, and the fact that we can reproducibly image the microgel surface (figure 1), even following a high-force map, indicates the microgel is being locally deformed rather than

penetrated. The Hertz model takes the form:

$$F = \frac{4}{3} \frac{(R_{eff})^{1/2} E}{(1 - v^2)} (h - h_0)^{3/2} \qquad (3)$$

where F is the applied force, E is the Young's modulus, h is the tip indentation, h_0 is the indentation at first contact between particle and tip (characterised by an initial increase in measured force) and v is the Poisson ratio.

We assume a value of $v = 0.4$, which has previously been determined for pNIPAM microgel particles,[45] accepting that this value was determined for significantly larger ($100 \mu m$) PNIPAm-based crosslinked microgel particles. The Poisson ratio could vary with particle size and with CMR, therefore propagating an error to any resulting value of E. Based on previous work[19, 21] it is reasonable to assume that the Poisson ratio is situated within a range $0.25 < v < 0.4$, which translates to a maximum error in any determined value of E of 11%. Finally, R_{eff} is the effective radius, calculated from the cantilever tip radius R_{tip} and the particle radius R as:

$$R_{eff} = \frac{1}{\frac{1}{R} + \frac{1}{R_{tip}}} \qquad (4)$$

Because the Hertz model assumes the indentation of a flat plane, rather than a sphere, the use of an effective radius compensates for the curvature of the microgel particle in calculating the modulus. R is approximated by using the measured particle hydrodynamic radii from DLS as shown in figure S1 and we measure R_{tip} separately for each experiment to account for manufacturing variabilities and tip degradation over time.

Finally, to ensure the validity of the Hertz model and to minimise the influence of the stiff underlying substrate on modulus calculations, it is generally accepted that moduli must be calculated within the limit of small indentations, typically cited as <

20%.[46] However the highly deformable nature of the particles and the variability of moduli between particles of different CMRs result in large variations in indentation such that using a consistent indentation range was not feasible. The moduli were instead calculated within the limit of low applied force. A force range of 0-50pN, was chosen, which corresponds to the minimum region that displays a clear response fitting well to the Hertz model and also clearly rises above the baseline force noise of around +15pN.

Figure 2A shows an overlay of approximately 150 force curves, (raw data), with a similar number at each CMR displayed in different colours. Expanded views of the curves at each CMR, along with fit lines, are shown in Figure S4 in the supplementary information. In these plots, the colours of the force curves represent multiple curves that are acquired around the centre of a single microgel particle, with at least three different microgel particles plotted. Although there is a spread of moduli for each particle, the different coloured curves (different particles) overlap to a high degree, indicating there is little difference in modulus in the population at a single CMR. We find the fit to the Hertz model to be reasonable with a coefficient of determination $R^2 = 0.85 - 0.90$. Although this can be artificially improved by using more free parameters in the fit, it can lead to significant variations in apparent moduli which are clearly not evidenced by the progression of the overlaid force curves in figure 2A. The high degree of thermal fluctuation noise from the unprocessed raw force curve data used also contributes to the lower than expected R^2.

An additional feature of the force curves at high CMR worth noting is a small attractive interaction just before contact, a so-called "jump-to contact" phenomenon, which leads to an initial decrease in the force curve before a subsequent increase during sample indentation.[47] Here, tip-sample intermolecular forces can exceed the cantilever's spring constant at short range and cause the tip to jump on to the surface. This phenomenon can be most clearly seen for the 6× particles but is also more subtly present for the 4× particles (figure 2A). This small attractive force is unlikely to be due to electrostatic forces as both the silicon probe and microgel have a very weak negative charge in water. A possible explanation is that the effect is caused by the denser particles having a higher polymer concentration near the surface exerting higher Van-der-Waals forces at small tip-sample separation. This hypothesis is supported by increased measured adhesion forces for higher CMRs following contact. We define adhesion force as the maximum negative force from retraction curves, giving forces of 535±20.7pN, 311±20.4pN and 66±10.8 for 6×, 4× and 2× particles respectively and negligible adhesion forces for 1× particles. The force associated with "jump-to contact" (13pN for the 6× particles) is barely higher than the AFM's force resolution; thus it can be assumed that its influence on the measured particle modulus is minimal.

The moduli of the microgel particles are determined to be within the range 3-40kPa, (figure 2B) with the measured moduli increasing monotonically with CMR, as expected. Error bars are larger for particles with higher CMRs, a consequence of their higher moduli which results in a narrower range of indentation data within the 0-50pN force range from which moduli were extracted, which in turn results in reduced statistics. Moduli are

observed to increase with a power law of exponent 3. This non-linear variation in calculated modulus is likely to be the result of the significant radial dependence of crosslink concentration and thus polymer segment concentration for low CMR microgels in comparison to high CMR microgels. Calculated moduli are of the same order of magnitude to those previously reported using 1μm colloidal probes.[26] This agreement with previously reported results supports the validity of our approach. The elastic moduli for each CMR are given in Table 1, with the stated error being the standard deviation of the individual force curves, with single particle variability and between particle variability both propagated.

We take advantage of the precise knowledge of the applied forces, by characterising how the height profile collapses with increasing imaging force. The absolute particle indentations $(h - h_0)$ across the particle are used to give the particle shape at increasing applied force, using the same data and analytical approach as in figure 2. Radial profiles are extracted from the force curves perpendicular to the tip-scan direction and plotted normalised to the initial height in figure 3 (see also figure S5 of the supplementary information, which depicts plots of normalised height at the particle centre versus the applied force). Clear qualitative differences can be observed in the cross-sectional compression upon increasing force. For the particles with the lowest CMR (1×), the peak height is shown to reduce by 90% at 400pN, whereas for the same force, the 6× particles reduce in height by only 20%. Additionally, the initial deformation (0-100pN) is by far the most pronounced for the particles with the lowest CMRs. From these results we draw two conclusions: 1) the AFM tip is able to distinguish a radial mechanical heterogeneity in the internal structure of the particles and 2) this heterogeneity is significantly more pronounced for particles with lower CMRs, indicating a more pronounced radial variation in particle mechanics.

3.4 Peak Force QNM

Force mapping is implemented at higher speeds using Peak Force Quantitative Nanomechanical Mapping (PF-QNM), in which high frequency force curves are analysed in real time to give high resolution topographical and nanomechanical maps of material properties with a fine control over force. As well as the sample height, PF-QNM analysis also reveals the local elastic modulus, the local deformation induced by the cantilever tip and the adhesive force between tip and sample. A representative area containing 6× microgel particles is shown in figure 4, which depicts the height (A), the elastic modulus (B), the tip-induced deformation (C) and the tip-sample adhesion (D), respectively. The elastic modulus is captured logarithmically to maximise the dynamic range due the large difference in elastic response between the microgel particles and the silicon substrate. As a result, small local differences in particle modulus cannot be easily resolved in the elastic modulus channel. However the particle appears larger in the elastic modulus channel than in the height channel indicating that the particle periphery is too soft to be observed in the height channel but clearly resolvable in the elastic modulus channel. The measured adhesion, defined as the pull-off force of the cantilever tip, is observed to vary radially across each particle, which we
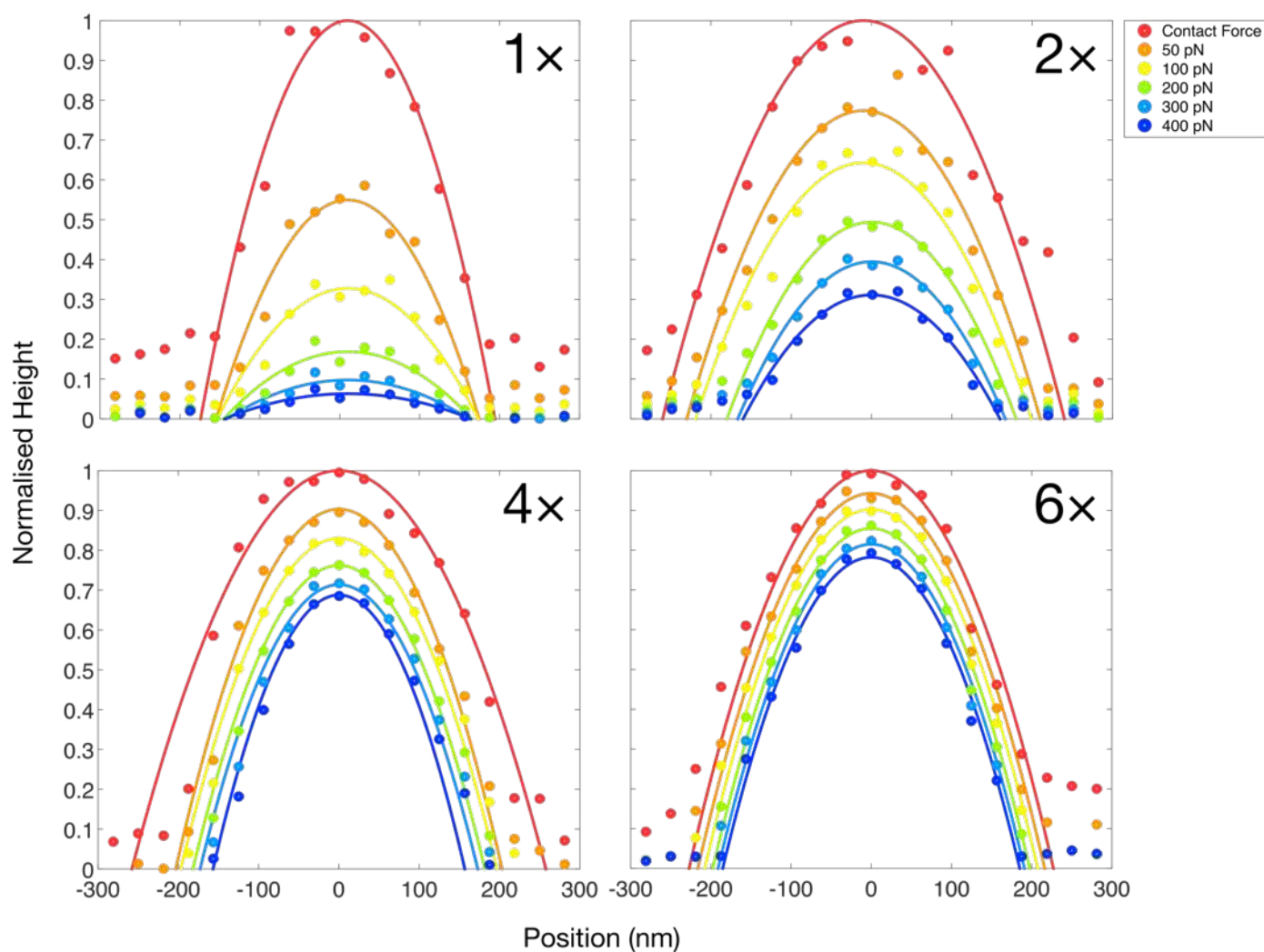
Fig. 3 Relative height profile of individual particles prepared with variable CMR at increasing applied force, calculated from force- indentation curves. Solid lines show a quadratic fit to data. For each particle, relative compression is highest directly following the point of first contact, suggesting a soft particle outer layer. Relative compression from initial height is highest for 1x crosslinked particles ($\approx 90\%$ at 300pN) and is clearly observed to decrease with increasing CMR.

interpret to be a result of an increased contact area between the cantilever tip when a softer region is probed, leading to a higher adhesive force. The radial variation within particles is most significant, however, in the deformation measurement , with the image exhibiting a bright ring around the particle centre, indicating a significantly higher deformation at the particle periphery compared to the particle centre. This radial variation in mechanical response suggests a "core-corona" internal particle structure, where the "core" of the particle exhibits a low deformation and the outer "corona" exhibits a more pronounced deformation. We also observe a slight particle deformation in the x-direction (parallel to the scan). The marked contrast between particle core and periphery and the lateral extent of this heterogeneity, particularly in the deformation channel, eliminates, in our view, the possibility that the phenomenon could be attributed to common artefacts in AFM data such as edge artefacts from tip deconvolution.[48]

PF-QNM force curves are fitted in real time using the Derjaguin, Muller, Toropov (DMT) model, with the peak force set to 200pN.

Given the high disparity in modulus between the soft particles and the hard substrate, the modulus is captured in logarithmic increments. Peak Force QNM extracts moduli from a force range of 10-70% of the full unloading force curve, a wider range than the small deformations that are used when calculating the modulus in force mapping. This means that, for mechanically heterogeneous particles, the measured moduli represents the mechanical response of a deeper region of the particles' internal structures (closer to the particle cores), averaged over a broader range of indentations. As shown in table 1, we find that the moduli when measured in this way are up to 5 times higher than those reported in figure 2, further evidence that the particle core is significantly stiffer than the corona.

To further test the accuracy and limits of PF-QNM the force was varied within the range of 50pN to 1000pN, capturing particle height profiles at variable force, analogous to the force-volume profiles shown in figure 3. Averaged particle cross sections captured in this way are shown in figure S6 of the supplementary in-

Table 1 Youngs Modulus from Force Volume and PF-QNM. Force volume moduli are calculated from small indentations, representing the particle "corona", while PF-QNM moduli are calculated from high indentations representing the particle "core". Errors in Force Volume are standard deviations, reflecting deviations between particles.

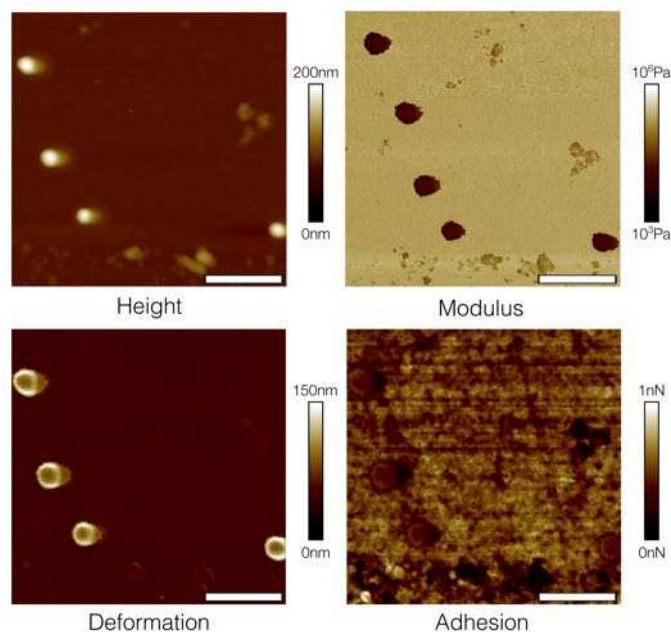| CMR	1×	2×	4×	6×
Force-Volume (kPa)	3.08±1.18	4.95±0.37	13.10±0.74	32.60±4.50
PF-QNM (kPa)	17.1	29.6	20.8	48.3

Fig. 4 Peak force quantitative nanomechanical mapping (PF-QNM) micrographs at 200pN showing the height, log modulus, tip-induced sample deformation and tip-sample adhesive force. The particle diameter appears smaller in the height micrograph than in the other three channels, demonstrating that particle compression varies radially, even at low forces. This is also characterised by a non-uniform radial distribution in the deformation channel, and to a lesser degree, the log modulus and adhesion channels.

Fig. 5 PF-QNM micrographs of individual microgel particles at an imaging force on 1000pN. At this force the particles are fully compressed, giving a purely qualitative picture of the radial deformation, adhesion and modulus. At 1× CMR (bottom line), the particles are too soft to register a mechanical response at this high force, however for higher CMRs (lines 1-3) a nonuniform radial profile is clearly visible across multiple channels, showing a softer, more adhesive and more deformable particle periphery and a harder particle core.

formation. From adding the measured deformation to measured height, the height at zero force is found to be 135±24nm, of similar magnitude to the height of 151±8nm measured with low force contact mode as shown in figure S2 of the supplementary information.

At the highest applied forces, nonlinear effects mean that particle deformations are no longer Hertzian. However, the contrast between the mechanical response at the particle centre and periphery is amplified, thereby providing a qualitative indication of the internal particle mechanical structure. As shown in figure 5, the characteristic "core-corona" profile, observed in the linear regime at the highest CMR (6×) is now even more pronounced and is also observed at lower CMRs: 4× and 2×. The lowest CMR, 1×, however does not show this distinction, an observation we attribute to the significantly softer response of these particles both at the particle core and at the periphery making the internal mechanical profile difficult to resolve.
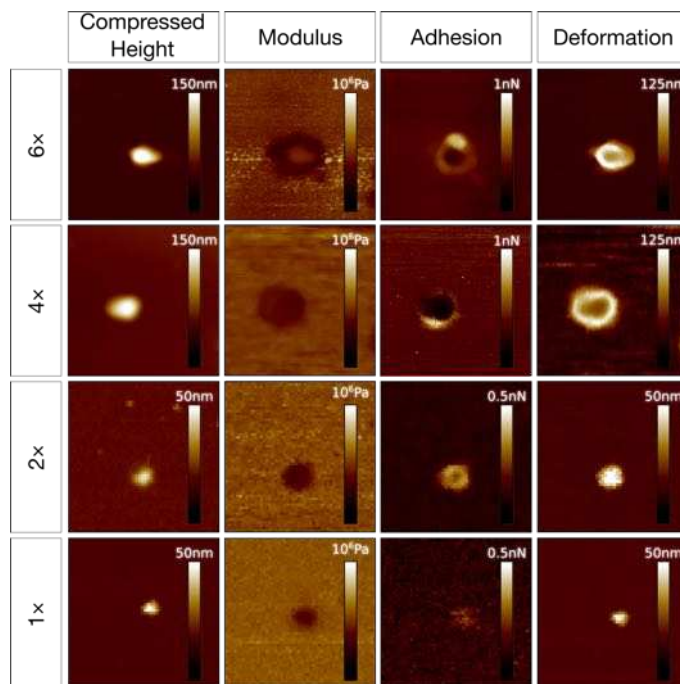
4 Discussion

Combining the findings above from different AFM modes leads us to propose an internal structural profile for each of the four microgel particle batches. For all of the particles studied here, their mechanical response is clearly shown to vary radially. We propose a radial model of this structure based on three regimes of mechanical response within the particles, as outlined in figure 6.

The core of the particle is generally accepted to have the highest polymer density, a consequence of the emulsion polymerisation method: as the particle grows outward the CMR increases.[49] When probed using contact mode AFM (figure 1), even at higher forces and with the lowest CMRs, the centre of the particle retains a measurable height. Further evidence of this can be found in the particle cross-sections as determined from force-distance curves (figure 3) where, at the highest applied forces, the particle compresses to an unresolvable height at it's periphery but maintains a measurable profile at its centre, varying from just 9.7% of the
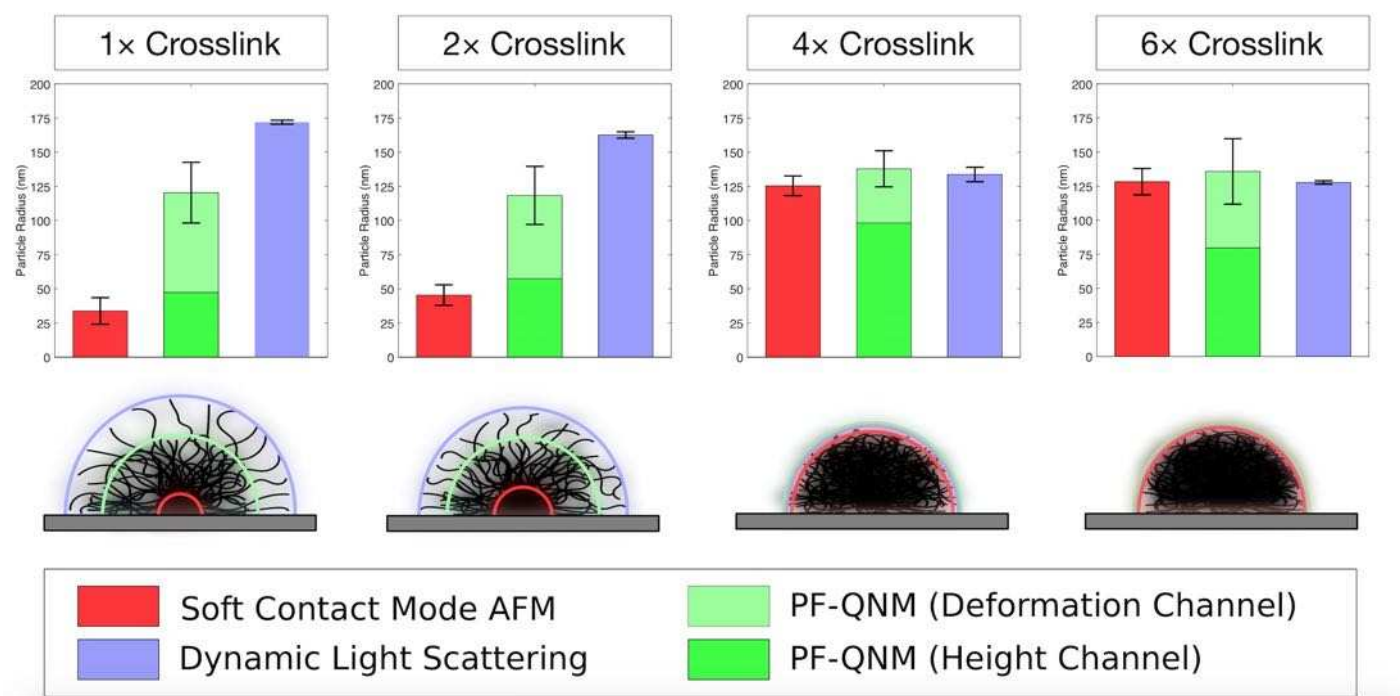
Fig. 6 Data from contact mode AFM, PF-QNM and DLS provide a comprehensive picture of the radii of the different regimes characterising the microgel mechanical properties (top). DLS data provide a measure of the outer periphery of the particles. Contact mode AFM probes the stiffest region of the particles, the "core" while PF-QNM probes the softer outer "corona" of the particles. Increasing the CMR results in a larger core radius and a reduced corona (bottom).

initial height for the lowest CMR to 81.5% of the initial height for the highest CMR. From this we can surmise that increasing the particle CMR is directly linked to an increase in the radial extent of this stiff particle core. As an approximation of the radius of this stiff core, we use the heights measured by low force contact mode AFM as an approximation of the radius of this stiff core. In reality, this may slightly underestimate the extent of this stiff core, as the force may cause the core to deform.

Outside this core, the particles' mechanical responses are more compliant, as demonstrated by their increased compressibility with applied force. This suggests an internal structure similar to the reported "core-corona" model[50] of microgel structure. For the purposes of this study we define the full radial extent of the particle, including both core and corona, as the averaged particle height when the force applied is extrapolated to zero, as shown in figure S6 of the supplementary information. This height is taken from PF-QNM rather than force-volume mode AFM due to its higher throughput, resulting in better statistics for the purposes of averaging. Our definition of this combined radius thus represents the highest radial extent of the particle that can be measured using nanoindentation. While this threshold is technique-dependent, it does provide a consistent measure of height that allows comparison between different CMRs. As well as height data, both force-volume mode (figure 3) and PF-QNM (figure 4) show this shell in the lateral dimension, with a particularly striking distinction in the deformation channel of PF-QNM. While the distinction between core and shell is clearly recognisable for the highest CMR at low force, when compressive forces are increased (figure 5) this difference in compressibility also becomes appar-

ent for particles with lower CMRs. This is an indication that the increased indentation begins to probe sufficiently deeply into the particle to distinguish the stiff core from the softer shell. Interestingly the average radial extent of the shell appears to be approximately constant for all particles, once error bars from inter-particle variability are taken into account, suggesting that the main effect of increasing the CMR is to increase the size of the stiff particle core, whose radius ranges from 34nm for the $1\times$ particles to 128nm for $6\times$ particles. For the $6\times$ particles the measured core and shell radii are similar indicating a much less pronounced degree of heterogeneity, although the visual evidence of a corona in figure 4 suggests that some degree of heterogeneity remains. Across all particle CMRs, the modulus measured using force volume AFM is significantly lower than the modulus measured by PF-QNM with the largest discrepancy between the two approaches observed for the $1\times$ particles. This discrepancy has a number of possible causes, related to the difference in indentation depth between the two approaches. Our force volume AFM probed the microgels at low deformations, representing the particle shell whereas PF-QNM probes a broader spectrum of deformations, including the particle core. We believe the discrepancies between techniques are therefore reflective of the differential mechanics between the particle periphery and particle core and that the $1\times$ CMR particles exhibiting the highest difference. However, we do not rule out other contributing factors. PF-QNM moduli are extracted solely from the cantilever's retraction curve and at significantly faster loading rates. This leaves open the possibility of differences in timescale-dependent phenomena between the samples such as relaxation. Examination of extension and retraction

curves revealed no hysteresis showing that a viscoelastic response is not detectable in this quasi-static regime (tip velocity $5\mu m s^{-1}$). PF-QNM is undoubtedly faster and could lead to an increased dissipative response from the microgel, although with a non-linear sinusoidal ramp (150nm at 250Hz) it is difficult to define a contact velocity.

Finally, the hydrodynamic radii R_h of the particles are probed using dynamic light scattering. The measured hydrodynamic radii align closely with the measured radii of the corona for the $4\times$ and $6\times$ particles but deviate significantly from this value for lower CMR particles. For the lower CMRs, the outermost extent of the particles therefore have a very weak mechanical response compared to the particle core, an observation supported by the fact that the measured moduli at the core and at the particle periphery (table 1) deviate for lower CMRs. Significantly, calculated moduli at the periphery are shown to give similar results to studies in which colloidal probe were used[26] but with the advantage of improved lateral resolution.

Neutron scattering and light scattering studies in the literature have previously attempted to quantify the ratio between the dense particle core and the less-dense corona. Differences between polymerisation protocols mean that a range of reported values exist, reflecting a range of particle sizes, CMRs and operating temperatures. This makes it difficult to correlate our findings directly with previously published work. The ratio between core and R_H is generally reported to be relatively high ($\sim 60\%$[31]-80%[30]) for particles that correspond most closely to the $4\times$ particles that we report here. For this CMR we measure a ratio between core radius and R_H of $\sim 90\%$, which is qualitatively similar and in approximate quantitative agreement with these previous studies.

5 Conclusions

In this article we demonstrate that, using thermally stable cantilevers and appropriate AFM imaging techniques and parameters, it is possible to image and nanoindent soft microgel particles without compromising image resolution. Furthermore, this allows for a quantitative measure of the spatial variation of particle elasticity. The ease by which PNIPAm particles and other microgels can be modified structurally and mechanically is well established. Here, we show how this tunability extends to the particles' internal radial elastic profile. Combining different modes of AFM nanoindentation with dynamic light scattering leads to the identification of three radially distinguishable regions of different mechanical response, in agreement with a core-corona model of radial structure. This model of microgel internal structure has been previously used as an approximation for both experimental[50,32] and simulation[51] studies. Our results are in good agreement with these studies and thus further validate the core-corona model, presenting the opportunity for future studies that could, for example, correlate such results with theoretical models of radial polymer density or other established experimental techniques.

The two modes of nanoindentation, force-volume and Peak Force QNM, are shown to be effective within the kPa modulus range. Force volume data from low indentations of the extension curve probes the outer "corona" of the particle and PF-QNM data from the retraction curve probes the mechanics closer to the particle core. We find a systematic variation of the determined elastic moduli at the particle core with the crosslink concentration set during synthesis where the elastic Young's modulus varies from 17-48kPa, as measured by Peak Force QNM. This radial variation is also manifested in the particle corona, where the elastic Young's modulus varies from 3-40kPa. Notably, for the more densely crosslinked particles ($4\times$ and $6\times$), we observe similar moduli, which is a consequence of their significantly lower radial heterogeneity. Being able to measure and control this radial profile could have interesting implications for numerous industrial applications where radial polymer density plays an important role such as tuning microgels porosity for controlled release[52] or in adapting particle architecture to achieve structural colour.[53]

We believe that our results validate the use AFM tips with small radii for nanoindentation, in contrast to more commonly used colloidal probes. The use of such tips avoids the common trade-off between increasing lateral resolution and ensuring low contact forces. The key factors in this approach are AFM cantilever stability, low spring constant and in the case of PF-QNM the use of the lowest possible loading rates. The moduli of the particles studied here are of similar order of magnitude to the softest biological tissues, which suggest that these techniques should be equally applicable in such contexts. The key technical aspect of our approach involves the use of highly stable cantilevers that are not susceptible to thermal drift. The present developments towards even higher cantilever stability by technical advances such as AFM stage stabilisation,[54] cantilever modifications,[55] and precise tip position determination[56] provide a diversity of potential routes to even higher probe stability. We anticipate that these continuing advances will lead to the ability to carry out quantitative mechanical characterisation of materials with even softer mechanical responses.

References

1 R. Pelton, *Advances in colloid and interface science*, 2000, **85**, 1–33.

2 A. Pich and W. Richtering, *Chemical design of responsive microgels*, Springer, 2010, vol. 234.

3 M.-J. Zhang, W. Wang, R. Xie, X.-J. Ju, L. Liu, Y.-Y. Gu and L.-Y. Chu, *Soft Matter*, 2013, **9**, 4150–4159.

4 M. Laurenti, E. Lopez-Cabarcos, F. Garcia-Blanco, B. Frick and J. Rubio-Retama, *Langmuir*, 2009, **25**, 9579–9584.

5 M. Zeiser, I. Freudensprung and T. Hellweg, *Polymer*, 2012, **53**, 6096–6101.

6 K. Geisel, L. Isa and W. Richtering, *Langmuir*, 2012, **28**,

15770–15776.

7   A. Sarkar, F. Kanti, A. Gulotta, B. S. Murray and S. Zhang, *Langmuir*, 2017, **33**, 14699–14708.

8   D. M. Headen, J. R. García and A. J. García, *Microsystems & Nanoengineering*, 2018, **4**, 17076.

9   S. Schmidt, M. Zeiser, T. Hellweg, C. Duschl, A. Fery and H. Möhwald, *Advanced Functional Materials*, 2010, **20**, 3235–3243.

10 A. Fernandez-Barbero, A. Fernandez-Nieves, I. Grillo and E. Lopez-Cabarcos, *Physical Review E*, 2002, **66**, 051803.

11 A. Fernandez-Nieves, H. Wyss, J. Mattsson and D. A. Weitz, *Microgel suspensions: fundamentals and applications*, John Wiley & Sons, 2011.

12 G. L. Hunter and E. R. Weeks, *Reports on Progress in Physics*, 2012, **75**, 066501.

13 T. Hellweg, C. Dewhurst, E. Brückner, K. Kratz and W. Eimer, *Colloid & Polymer Science*, 2000, **278**, 972–978.

14 Z. Wang, A. M. Alsayed, A. G. Yodh and Y. Han, *The Journal of chemical physics*, 2010, **132**, 154501.

15 Z. Zhang, N. Xu, D. T. Chen, P. Yunker, A. M. Alsayed, K. B. Aptowicz, P. Habdas, A. J. Liu, S. R. Nagel and A. G. Yodh, *Nature*, 2009, **459**, 230.

16 P. Yunker, Z. Zhang, K. B. Aptowicz and A. G. Yodh, *Physical review letters*, 2009, **103**, 115701.

17 A. Basu, Y. Xu, T. Still, P. Arratia, Z. Zhang, K. Nordstrom, J. M. Rieser, J. Gollub, D. Durian and A. Yodh, *Soft matter*, 2014, **10**, 3027–3035.

18 J. R. Seth, L. Mohan, C. Locatelli-Champagne, M. Cloitre and R. T. Bonnecaze, *Nature materials*, 2011, **10**, 838.

19 H. M. Wyss, J. Mattsson, T. Franke, A. Fernandez-Nieves and D. A. Weitz, *Microgel Suspensions: Fundamentals and Applications*, 2011, 311–325.

20 J. Mattsson, H. M. Wyss, A. Fernandez-Nieves, K. Miyazaki, Z. Hu, D. R. Reichman and D. A. Weitz, *Nature*, 2009, **462**, 83.

21 H. M. Wyss, T. Franke, E. Mele and D. A. Weitz, *Soft Matter*, 2010, **6**, 4550–4555.

22 O. Tagit, N. Tomczak and G. J. Vancso, *Small*, 2008, **4**, 119–126.

23 A. Burmistrova, M. Richter, C. Uzum and R. v. Klitzing, *Colloid and Polymer Science*, 2011, **289**, 613–624.

24 J. Wiedemair, M. J. Serpe, J. Kim, J.-F. Masson, L. A. Lyon, B. Mizaikoff and C. Kranz, *Langmuir*, 2007, **23**, 130–137.

25 T. Matzelle, G. Geuskens and N. Kruse, *Macromolecules*, 2003, **36**, 2926–2931.

26 S. M. Hashmi and E. R. Dufresne, *Soft Matter*, 2009, **5**, 3682–3688.

27 T. Mason and M. Lin, *Physical Review E*, 2005, **71**, 040801.

28 F. Schneider, A. Balaceanu, A. Feoktystov, V. Pipich, Y. Wu, J. Allgaier, W. Pyckhout-Hintzen, A. Pich and G. J. Schneider, *Langmuir*, 2014, **30**, 15317–15326.

29 M. Ballauff and Y. Lu, *Polymer*, 2007, **48**, 1815–1823.

30 M. Reufer, P. Dıaz-Leyva, I. Lynch and F. Scheffold, *The European Physical Journal E*, 2009, **28**, 165–171.

31 M. Stieger, W. Richtering, J. S. Pedersen and P. Lindner, *The Journal of chemical physics*, 2004, **120**, 6197–6206.

32 G. M. Conley, S. Nöjd, M. Braibanti, P. Schurtenberger and F. Scheffold, *Colloids and Surfaces A: Physicochemical and Engineering Aspects*, 2016, **499**, 18–23.

33 J. Adamcik, C. Lara, I. Usov, J. S. Jeong, F. S. Ruggeri, G. Dietler, H. A. Lashuel, I. W. Hamley and R. Mezzenga, *Nanoscale*, 2012, **4**, 4426–4429.

34 L. Picas, F. Rico and S. Scheuring, *Biophysical journal*, 2012, **102**, L01–L03.

35 A. Aufderhorst-Roberts, U. Chandra and S. D. Connell, *Biophysical journal*, 2017, **112**, 313–324.

36 G. Pletikapić, A. Berquand, T. M. Radić and V. Svetličić, *Journal of phycology*, 2012, **48**, 174–185.

37 H. Senff and W. Richtering, *The Journal of chemical physics*, 1999, **111**, 1705–1711.

38 B. J. Frisken, *Applied Optics*, 2001, **40**, 4087–4091.

39 J. L. Hutter and J. Bechhoefer, *Review of Scientific Instruments*, 1993, **64**, 1868–1873.

40 D. E. Koppel, *The Journal of Chemical Physics*, 1972, **57**, 4814–4820.

41 G. Duplatre, M. Ferreira Marques and M. da Graça Miguel, *The Journal of Physical Chemistry*, 1996, **100**, 16608–16612.

42 H. Schillers, C. Rianna, J. Schäpe, T. Luque, H. Doschke, M. Wälte, J. J. Uriarte, N. Campillo, G. P. Michanetzis, J. Bobrowska *et al.*, *Scientific Reports*, 2017, **7**, 5117.

43 M. Garcia, K. D. Schulze, C. S. OâĂŹBryan, T. Bhattacharjee, W. G. Sawyer and T. E. Angelini, *Tribology-Materials, Surfaces & Interfaces*, 2017, 1–6.

44 D. C. Lin, E. K. Dimitriadis and F. Horkay, *Journal of biomechanical engineering*, 2007, **129**, 430–440.

45 P. Voudouris, D. Florea, P. van der Schoot and H. M. Wyss, *Soft Matter*, 2013, **9**, 7158–7166.

46 N. Gavara and R. S. Chadwick, *Nature nanotechnology*, 2012, **7**, 733–736.

47 H.-J. Butt, B. Cappella and M. Kappl, *Surface science reports*, 2005, **59**, 1–152.

48 U. Schwarz, H. Haefke, P. Reimann and H.-J. Güntherodt, *Journal of Microscopy*, 1994, **173**, 183–197.

49 T. Hoare and D. McLean, *Macromolecular theory and simulations*, 2006, **15**, 619–632.

50 F. Scheffold, P. Díaz-Leyva, M. Reufer, N. B. Braham, I. Lynch and J. L. Harden, *Physical review letters*, 2010, **104**, 128304.

51 N. Gnan, L. Rovigatti, M. Bergman and E. Zaccarelli, *Macromolecules*, 2017, **50**, 8777–8786.

52 Y. Gao, K. Y. Wong, A. Ahiabu and M. J. Serpe, *Journal of Materials Chemistry B*, 2016, **4**, 5144–5150.

53 C. E. Finlayson and J. J. Baumberg, *Polymer International*, 2013, **62**, 1403–1407.

54 S. Sevim, S. Tolunay and H. Torun, *Microsystem Technologies*, 2015, **21**, 1559–1566.

55 D. T. Edwards and T. T. Perkins, *Journal of structural biology*, 2017, **197**, 13–25.

56 G. M. King, A. R. Carter, A. B. Churnside, L. S. Eberle and T. T.

Perkins, *Nano letters*, 2009, **9**, 1451–1456.